

Thermal Marangoni natural convection enables directional transport across immiscible liquids

Received: 5 December 2024

Accepted: 4 June 2025

Published online: 01 July 2025

Jiguang Wang¹, Lunxiang Zhang¹✉, Aliakbar Hassanpouryouzband²,
Xiang Sun³, Yu Liu¹, Jiafei Zhao¹ & Yongchen Song¹✉

The ability to control molecular transport across immiscible liquid interfaces is critical for applications in manufacturing, biotechnology, and space research. Such transport mechanisms have garnered attention for their intriguing behavior and transformative potential in technology and science for a long time. Here, we demonstrate that unsteady temperature fields drive directional transport of water molecules across the oil-water interface, where weakened hydrogen bonding orients hydroxyl groups toward the oil phase. Through the Marangoni natural convection, water molecules migrate into the oil phase, forming stable nanoscale dispersions. We provide evidence that this transport is tunable via temperature gradients, offering a controllable pathway for mass transfer. This approach offers a potential, scalable, surfactant-free method for nanoemulsions production, with applications in drug delivery and advanced manufacturing. With surface tension as one of the driving forces, this phenomenon is equally valid in microgravity or zero-gravity environments. These findings advance the understanding of Marangoni natural convection and provide new insights into microscale fluid dynamics and spontaneous molecular migration at the oil-water interface.

From manufacturing to drug delivery, the controlled transport of molecules across liquid interfaces is a cornerstone of modern science. However, existing methods often rely on surfactants, limiting their scalability and environmental compatibility. Multicomponent fluid dynamic systems are ubiquitous in both nature and technology, characterized by complex fluid interfaces and non-equilibrium physical fields¹. Temperature, pressure, and concentration gradients at these interfaces drive directional molecular transport to restore equilibrium. This directional transport mediates various physical and chemical phenomena within and between the liquids², attracting significant scientific and technological interest. For example, when two immiscible and unequilibrated liquids are in contact, molecular transfer across the interface occurs due to chemical potential gradients, a phenomenon known as spontaneous emulsification that is

used in emulsion production³. Directional transport is also inducible by surface tension gradients, as demonstrated in the solute Marangoni effect^{4,5}, originally observed in wine tears⁶. This effect explains diverse phenomena, such as the self-propulsion of insects and the formation of ring stains in dried coffee drops^{7,8}. It has found applications in inkjet printing⁹, droplet manipulating^{10–12}, surface cleaning¹³, and ordered pattern generation^{2,14}. However, these technologies often require surfactants to achieve controlled directional transport, which inevitably results in the introduction of one or more chemicals into the system. These chemicals can contaminate systems and limit their practical utility.

Addressing these limitations requires innovative approaches leveraging natural fluid dynamics. Unlike solute concentration gradients, temperature gradients induce flows without altering the

¹Key Laboratory of Ocean Energy Utilization and Energy Conservation of the Ministry of Education, Dalian University of Technology, Dalian, China. ²School of GeoSciences, University of Edinburgh, Edinburgh, UK. ³Institute of Rock and Soil Mechanics, Chinese Academy of Sciences, Wuhan, China.

✉ e-mail: lunxiangzhang@dlut.edu.cn; songyc@dlut.edu.cn

liquid composition. When a non-uniform temperature field exists on a liquid interface, surface tension gradients drive fluid flow from warmer to cooler regions - the thermal Marangoni effect¹⁵. The thermal Marangoni effect is usually described within the Rayleigh–Bénard (R–B) convection framework, alternatively termed Rayleigh–Bénard–Marangoni (R–B–M) convection^{16,17}. Classical R–B–M system describes vertical temperature gradient formation in a single thin horizontal fluid layer (heated from below and cooled from above), leading to buoyancy-driven instability and ultimately inducing convection. Combined buoyancy and surface tension effects spontaneously generate organized convection structures (hexagonal or roll-shaped cells), driving the directional transport of liquid^{18–20}. Due to the fact that the interfacial convection is characterized by a variety of physical mechanisms and types of instability, Marangoni natural convection in oil-water two-layer systems can be more complex¹⁸. A mechanistic understanding of the underlying mutual influences and interactions between different interfaces is a prerequisite for successful applications of this phenomenon²¹. Various experimental and theoretical studies have been carried out to investigate the onset of the underlying instability and resulting pattern formation^{22–24}. Given the natural ubiquity of multilayer fluid systems, two-layer or multilayer Marangoni natural convection systems exhibit profound potential for practical applications in heat, mass, and momentum transport²⁵.

Here, we demonstrate the directional transfer of water molecules into the oil phase, driven by thermal Marangoni natural convection in an oil-water two-layer system. The time-dependent thermal boundary conditions in a confined geometry are utilized to establish a radially decaying temperature gradient. This gradient simultaneously induces buoyancy and surface tension gradients that synergistically drive convection. In the convection process, one stable centrifugally

rotating toroidal cell forms in the oil and water layers, respectively. Furthermore, there is a natural complex interaction between oil and water molecules at the oil-water interface where two toroidal cells contact each other. The weakened hydrogen bonding between interfacial and bulk water molecules drives spontaneous aqueous penetration into the oil phase. The synergy between toroidal convection patterns and interfacial molecular dynamics enables directional transfer of water molecules from water to the oil phase. These water molecules subsequently self-assemble into nanoscale droplets within the oil phase, forming water-in-oil nanoemulsions. By characterizing the movement and concentration of water molecules, this study introduces a scalable, surfactant-free solution for molecular transport in complex fluid systems.

Consider a system consisting of two layers of immiscible mineral oil and water (Fig. 1a). The variables referring to the top and bottom layers are denoted by the subscripts “o” and “w,” respectively. The upper surface of the two-layer system is in contact with air (oil-air interface), the bottom surface and the sides are in contact with walls. Because of the low thermal conductivity and viscosity of air, thermal and momentum exchanges between the air and oil phases are neglected. Moreover, in the absence of azimuthal gradients in both phases, and no circumferential flow was observed experimentally, the three-dimensional problem can be simplified to a two-dimensional axisymmetric problem. The geometric configuration and boundary conditions of the model are illustrated in Fig. 2a. The governing equations follow the formulation proposed by Simanovskii and Nepomnyashchy^{18,21}, comprising the Navier-Stokes equations and continuity equation for incompressible, non-isothermal laminar flow, together with energy equations that account for both convective and conductive heat transfer. The Boussinesq approximation is adopted to simplify the non-isothermal flow, as density variations are sufficiently

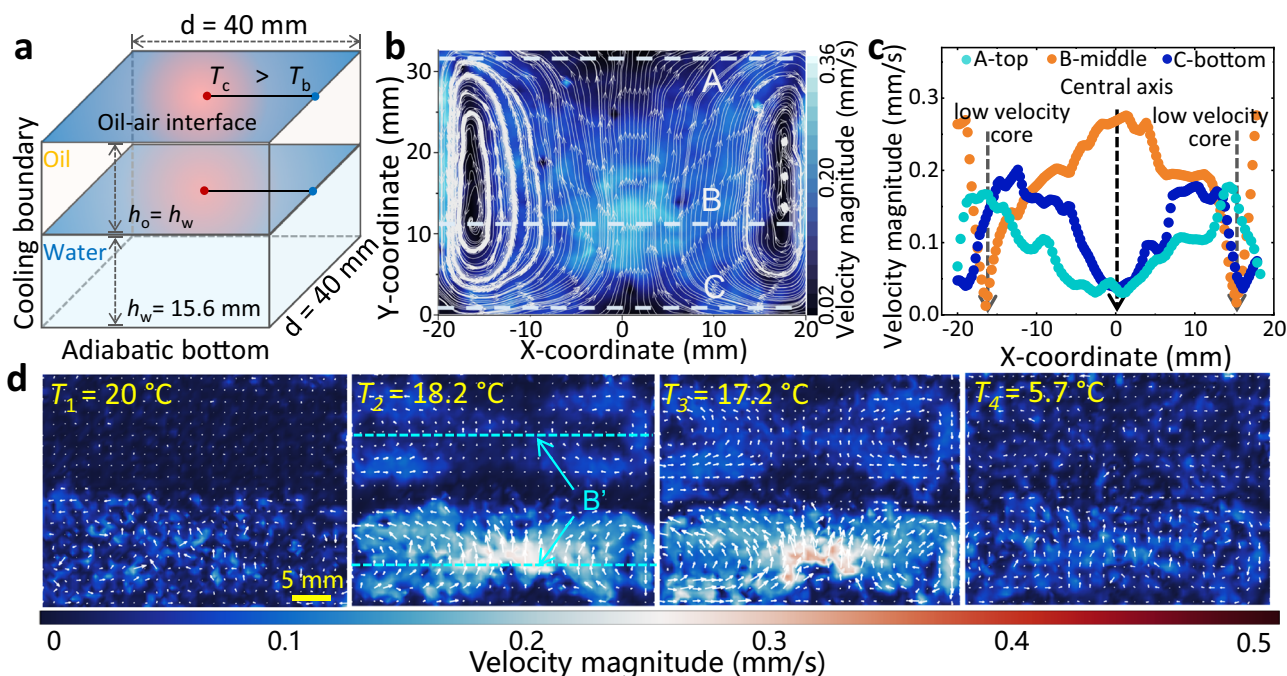


Fig. 1 | Marangoni natural convection within the liquids. **a** Sketch of the typical oil-water two-layer Marangoni convection system, where the subscripts “o” and “w” represent oil and water, and “c” and “b” represent center and boundary, respectively. T refers to the temperature, d refers to the length of the side, h refers to the height. Red and blue colors indicate high and low temperatures, respectively. Red and blue dots indicate the center and boundary, respectively. **b** Instantaneous pathline cloud map of the flow field at 13 °C in the deionized water cooling test. Axes denote flow field geometric dimensions. Three dotted lines indicate

monitoring lines at different depths. White lines are particle motion trajectories. Arrows denote flow direction. The gradient color bar denotes the velocity magnitude distribution. **c** Velocity magnitude distribution corresponding to the three monitoring lines in Fig. 1b. **d** Instantaneous cloud maps with different temperatures during oil-water cooling. The gradient color bar reflects the distribution of velocity magnitude. The lengths of vectors represent the relative magnitude of the velocity, and their direction indicates the flow orientation. Scale bar: 5 mm. Refer to the Methods section for detailed calculations.

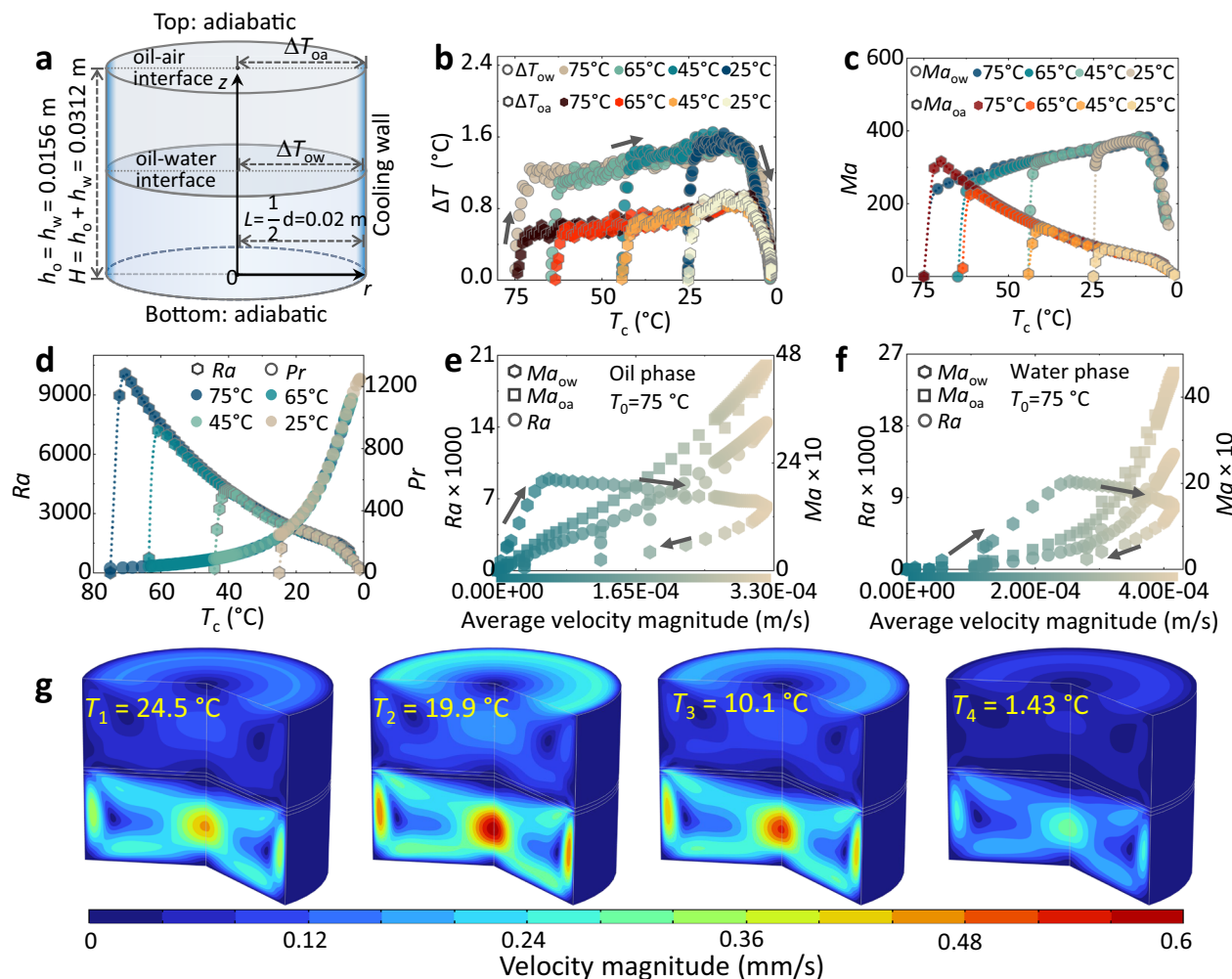


Fig. 2 | Modeling and dimensionless parameter analysis. **a** Schematic diagram of the mathematical model for Marangoni natural convection. The axisymmetric system uses cylindrical coordinates with adiabatic upper/lower boundaries. ΔT_{oa} and ΔT_{ow} are temperature differences between the center and the boundary at the oil-air/oil-water interfaces. h_o/h_w show oil/water layer thicknesses. H and L denote total height and characteristic length. Navy blue: cooling wall. Arrows: r/z -axes. **b** Experimentally measured interfacial temperature differences (ΔT_{ow} : circles, ΔT_{oa} : hexagons) versus their central temperature T_c during cooling. Color fills represent distinct initial temperatures ($T_0 = 75, 65, 45, 25^\circ\text{C}$). Arrows mark three cooling stages of ΔT evolution. **c** Evolution of Marangoni numbers (Ma_{ow} : circles, Ma_{oa} : hexagons) with T_c during cooling. Colors correspond to initial temperatures. Ma

values are calculated using experimentally measured thermophysical properties. **d** Evolution of Rayleigh (Ra : hexagons) and Prandtl (Pr : circles) numbers with T_c during cooling. Colors correspond to initial temperatures. Both Pr and Ra values are calculated using experimentally measured thermophysical properties. Numerically simulated spatial-average velocity magnitudes in oil (**e**) and water (**f**) flow fields versus dimensionless numbers (Ra : circles, Ma_{ow} : hexagons, Ma_{oa} : squares) under $T_0 = 75^\circ\text{C}$. Colors indicate velocity magnitudes. Color bars: velocity scales. Arrows mark the three ΔT stages from (**b**). **g** Schematic of cross-sectional flow field views at selected temperatures during cooling. The gradient color bar denotes velocity magnitude. The initial temperature is 25°C .

small. At the interfaces between phases, only surface tension variations induced by temperature gradients are considered, while the effects of pressure differences and concentration gradients are neglected. The nondimensionalization uses L ($L = 1/2 d = 0.02\text{ m}$) as the characteristic length scale, $U = \alpha_o/L$ (m/s) as the characteristic velocity, L^2/α_o (s) as the characteristic time, $\rho_o \alpha_o^2/L^2$ (Pa) as the characteristic pressure. Here, ρ_o (kg/m³) denotes the density of oil, and α_o (m²/s) denotes the thermal diffusivity of oil. Thermal diffusivity is defined as the ratio of thermal conductivity to the heat storage capacity, characterizing the propagation speed of temperature variations in the oil phase. The dimensionless temperature is defined as $T_i^* = \frac{T_i - T_b}{\Delta T_{oa}}$, where the subscript “ i ” represents the liquid (i =oil, water), the superscript “ $*$ ” denotes nondimensionalization, T_b is the boundary temperature, and ΔT_{oa} ($^\circ\text{C}$) is the temperature difference between the center and boundary across the oil-air interface. The nondimensional governing equations for both fluids have the following forms^{18,21}. For the upper oil phase, the

equations read:

$$\nabla \cdot \mathbf{u}_o^* = 0 \quad (1)$$

$$\frac{\partial \mathbf{u}_o^*}{\partial t^*} + \mathbf{u}_o^* \cdot \nabla \mathbf{u}_o^* = -\frac{\partial p_o^*}{\partial r^*} + Pr \nabla^2 \mathbf{u}_o^* \quad (2)$$

$$\frac{\partial \mathbf{u}_o^*}{\partial t^*} + \mathbf{u}_o^* \cdot \nabla \mathbf{u}_o^* = -\frac{\partial p_o^*}{\partial z^*} + Pr \nabla^2 \mathbf{u}_o^* + Ra Pr T_o^* \quad (3)$$

$$\frac{\partial T_o^*}{\partial t^*} + \mathbf{u}_o^* \cdot \nabla T_o^* = \nabla^2 T_o^* \quad (4)$$

where $\mathbf{u}_o^* = (u_{o,r}^*, u_{o,\theta}^*, u_{o,z}^*)$ are the velocity components in cylindrical coordinates (r, θ, z). Equations (2) and (3) are the momentum

equations in the r and z directions, respectively.

$$Pr = \frac{\nu_o}{\alpha_o} \quad (5)$$

where ν_o (m^2/s) is the kinematic viscosity of the oil phase. Pr is the Prandtl number corresponding to the ratio of the momentum and thermal diffusivities, and

$$Ra = \frac{g\beta_o\Delta T_{oa}L^3}{\nu_o\alpha_o} \quad (6)$$

is the Rayleigh number in which g (m/s^2) is the gravitational acceleration, and β_o ($1/^\circ\text{C}$) is the thermal expansion factor of the oil phase. Ra quantifies the relative strength of buoyancy-driven convection to viscous dissipation and thermal diffusion.

For the lower water phase, the equations read:

$$\nabla \cdot \mathbf{u}_w^* = 0 \quad (7)$$

$$\frac{\partial \mathbf{u}_w^*}{\partial t^*} + \mathbf{u}_w^* \cdot \nabla \mathbf{u}_w^* = -\frac{1}{\rho'} \frac{\partial p_w^*}{\partial r^*} + \nu' Pr \nabla^2 \mathbf{u}_w^* \quad (8)$$

$$\frac{\partial \mathbf{u}_w^*}{\partial t^*} + \mathbf{u}_w^* \cdot \nabla \mathbf{u}_w^* = -\frac{1}{\rho'_o} \frac{\partial p_w^*}{\partial z^*} + \nu' Pr \nabla^2 \mathbf{u}_w^* + \beta' Ra Pr T_w^* \quad (9)$$

$$\frac{\partial T_w^*}{\partial t^*} + \mathbf{u}_w^* \cdot \nabla T_w^* = \alpha' \nabla^2 T_w^* \quad (10)$$

The ratios of physical properties of the two fluid layers are defined as, $\rho' = \frac{\rho_w}{\rho_o}$, $\nu' = \frac{\nu_w}{\nu_o}$, $\beta' = \frac{\beta_w}{\beta_o}$, $\alpha' = \frac{\alpha_w}{\alpha_o}$. The boundary conditions associated with the governing equations are as follows:

$$r^*|_{z=(0, \frac{H}{L})} = 1, u_{w,r}^* = u_{w,z}^* = 0, T^* = 0 \quad (11)$$

$$r^*|_{z=(\frac{H}{L}, \frac{H}{L})} = 1, u_{o,r}^* = u_{o,z}^* = 0, T^* = 0 \quad (12)$$

$$z^* = 0, u_{w,r}^* = u_{w,z}^* = 0, \frac{\partial T_w^*}{\partial z} = 0 \quad (13)$$

$$z^* = \frac{H}{L}, u_{o,z}^* = 0, \frac{\partial T_o^*}{\partial z} = 0 \quad (14)$$

At the oil-air interface:

$$\frac{\partial u_{o,r}^*}{\partial z^*} = -Ma_{oa} \frac{\partial T^*}{\partial r^*} \quad (15)$$

$$Ma_{oa} = \frac{\gamma_{oa}\Delta T_{oa}L}{\mu_o\alpha_o} \quad (16)$$

At the oil-water interface:

$$\frac{\partial u_{o,r}^*}{\partial z^*} - \mu' \frac{\partial u_{w,r}^*}{\partial z^*} = -Ma_{ow} \frac{\partial T^*}{\partial r^*} \quad (17)$$

$$Ma_{ow} = \frac{\gamma_{ow}\Delta T_{ow}L}{\mu_o\alpha_o} \quad (18)$$

$$u_{w,r}^* = u_{o,r}^* \quad (19)$$

where μ_o (Pa.s) is the dynamic viscosity of oil, γ_{oa} and γ_{ow} (N/m °C) are the temperature coefficients of oil-air and oil-water interfacial tension, respectively. Ma is the Marangoni number, which represents the intensity of Marangoni forces with stabilizing viscous forces and stabilizing mass diffusion.

Results

Observation of Marangoni natural convection

A sapphire cubic reactor with thermally conductive sidewalls and a nearly adiabatic bottom, as detailed in the Methods section (Supplementary Fig. 1a, d, Supplementary Note 1), was employed for convection experiments. Figure 1a depicts the typical oil-water two-layer Marangoni convection system: 15.6 mm-thick (25 ml) oil/water (mineral oil/deionized water) layers in a 40 mm cubic domain, with sidewalls cooled from initial temperature ($T_o = 20/25/45/65/75^\circ\text{C}$) to 1°C at $12^\circ\text{C}/\text{h}$, a near-adiabatic bottom, and a 28.8 mm-thick top air layer. Distinct from classical Bénard convection, this system features dynamic thermal boundaries and lateral temperature gradients. To rigorously isolate convection patterns from biphasic effects, the evolution of flow fields in a controlled single-phase water system (31.2 mm thickness, $T_o = 20^\circ\text{C}$) during the cooling process (Supplementary Movie 1) was observed first.

The central vertical section of the flow field at 13°C (Fig. 1b) was obtained through a 2D particle image velocimetry (PIV) system (Supplementary Fig. 1a, Supplementary Note 1). The pathline cloud map and velocity magnitude profiles at three depths (Fig. 1c) indicate that the flow field is symmetrical, with ring-shaped circling structures (left rings counterclockwise, right rings clockwise) on both sides. Velocity magnitudes within both ring structures decay radially inward, peaking at the tangent region and diminishing to near-zero values at the cores. Both the top (dashed line A) and bottom (dashed line C) regions show analogous velocity magnitude distributions with a minimum at the center, while the boundary magnitude ($x = \pm 20$ mm) at the air-water interface slightly exceeds that near the solid-liquid interface. As a complement, the horizontal cross-sections of the flow field were qualitatively observed in a scaled-down system replicating equivalent thermal boundary conditions (Supplementary Fig. 1b, Supplementary Fig. 2, Supplementary Movie 2, Methods, Supplementary Note 2). The cloud map indicates that the top of the convection flows from the center to the boundary, whereas the direction is opposite at the bottom (Supplementary Fig. 2). The velocity magnitude decreases from the boundary to the center in both the top and bottom slices, corresponding to the pattern in Fig. 1c. Cross-sectional observations reveal that the fundamental Marangoni convection cell self-organizes into a symmetric toroidal topology, exhibiting radially outward flow dynamics.

Figure 1d illustrates the flow field evolution during the cooling of the oil-water two-layer system ($T_o = 20^\circ\text{C}$; experimental configuration in Fig. 1a). The oil and water phases remained stratified due to inherent density and polarity differences. Distinct symmetric toroidal convection cells with identical rotational directions emerged simultaneously in both layers (Supplementary Movie 3). Velocity magnitude and pathline maps (Supplementary Fig. 3, Supplementary Note 3) present the sequential formation and dissipation of toroidal structures during cooling. The velocity magnitude distributions of the biphasic convection cells (Supplementary Fig. 4c, Supplementary Note 3) matched those in the single-phase system (Fig. 1b). Nevertheless, contrasting thermophysical properties (e.g., viscosity(μ), thermal diffusivity(α)) between the phases induced higher peak velocity magnitude in the water layer. Temporal evolution of velocity magnitudes along the central monitoring lines B' (Fig. 1d, Supplementary Fig. 4a, b, Supplementary Note 3) demonstrates three distinct regimes: (i) weak stochastic fluctuations before thermal gradient establishment, (ii) acceleration phase culminating in maximum magnitude at about $T = 17.2^\circ\text{C}$, (iii) subsequent decay.

Table 1 | Specific numerical ranges of the dimensionless numbers

Initial Temperatures (°C)	Ra	Pr	Ma_{oa}	Ma_{ow}
25	0–2365.3	237.5–1247.9	0–76.4	0–371.8
45	0–4190	87–1118.4	0–134.7	0–388.7
65	0–7216.9	40.4–1092.6	0–230.1	0–377.3
75	0–10060	28.3–1065.8	0–319.1	0–388.2

Qualitatively, the cooling process establishes a horizontally decaying temperature gradient from the central region (T_c) to the boundary (T_b) (Fig. 1a), generating concurrent interfacial tension gradients at the oil-air and oil-water interfaces, while simultaneously establishing density gradients within both phases. Driven by interfacial tension gradients (Marangoni effect), substances migrate from high-temperature (center) to low-temperature regions (boundary). Concurrently, buoyancy-driven flow arises from density gradients, causing colder boundary fluids to sink and warmer central fluids to ascend. The synergistic interplay of these directional transport mechanisms establishes closed-loop convection pathways, centrifugal flow from the center to the boundary, followed by centripetal return via sub-surface transportation.

Numerical simulation validation

Numerical simulations were conducted based on the governing equations for the oil-water two-layer system. Linear triangular elements were employed to discretize the governing equations. A direct, fully coupled solver with a damped Newton iteration algorithm was used to solve the nonlinear equation system. The thermophysical properties of the mineral oil at various temperatures were measured experimentally and provided in Supplementary Fig. 6. To investigate the flow behavior driven by the spatiotemporal temperature variations, the temperature-velocity coupled governing equations were simplified to velocity-only equations by nondimensionalization at specific temperature points. Given the low temperature sensitivity of the material properties and the small temperature spatial variations during the experiment, both oil and water can be treated as homogeneous in viscosity and heat diffusivity at each specific temperature. The experimental results, which show no local convection arising from spatial variations in viscosity or heat diffusivity, validate this assumption (Fig. 1d). Density variations in the two-phase flow are accounted for via the Boussinesq approximation and buoyancy effects. The interfacial convection driven by temperature gradients is governed by the Marangoni effect.

To nondimensionalize the governing equations and obtain the nondimensional numbers, the temperature differences at any moment during cooling were required. The temperature differences at the oil-air and oil-water interfaces (ΔT_{oa} , ΔT_{ow}) were measured experimentally and expressed as piecewise functions (Supplementary Note 4) of the corresponding interface central temperature ($T_{c,oa}$, $T_{c,ow}$) under various T_0 conditions (Fig. 2b). The $\Delta T(T_c)$ curves for both interfaces exhibit similar three-stages with interface-specific magnitudes: (i) a rapid rise in ΔT under constant cooling (12 °C/h), as thermal inertia delays thermal equilibration; (ii) a gradual increase in ΔT driven by convective heat transfer; (iii) an abrupt collapse in ΔT post-cooling cessation. Given the small ΔT between the interfacial center and boundary at any moment “ t ” during the cooling process, the resulting density fluctuation $\Delta \rho \ll \rho_0$ in flow fields validates the application of the Boussinesq approximation.

In this Marangoni natural convection problem, Ra and Ma are two critical dimensionless parameters that govern buoyancy-driven convection in the bulk phase and the interface Marangoni effect, respectively. Through the experimentally measured thermophysical properties of the mineral oil and Eqs. (5), (6), (16) and (18), Ra , Pr ,

Ma_{oa} , and Ma_{ow} at all the temperature points during cooling under various initial temperatures were calculated (Fig. 2c, d, Table 1). Given the small instantaneous ΔT within the confined domain, spatially induced nonlinearities were neglected when determining the thermophysical properties at each temperature. The interface central temperature T_c was employed as the reference temperature for property evaluation.

The Ma_{oa} peaks rapidly during early cooling, driven by sharp ΔT_{oa} growth (Fig. 2b) during incipient convection. It then enters a viscous-dominated regime as the dynamic viscosity increases exponentially, and finally collapses as ΔT_{oa} decays. In contrast, the oil-water interface exhibits a nonlinear interfacial tension-temperature relationship ($\gamma_{ow}(T)$, Supplementary Fig. 6f). The cooling-induced γ_{ow} enhancement counteracts viscous resistance, sustaining Ma_{ow} growth until ΔT_{ow} collapse terminates convection (Fig. 2c). Although the attenuation of thermal diffusivity α_o during cooling enhances convection (Supplementary Fig. 6d), its maximum reduction (42.19% from 75 to 1 °C) is dwarfed by the 2303.07% increase in μ_o , manifesting as a surge in Pr (Fig. 2d). The Ra , reflecting buoyancy-driven convection intensity, exhibits an identical evolution pattern to Ma_{oa} . Rapid viscosity increase at lower temperatures is the primary convection restriction mechanism. In addition, numerical simulations of the flow fields confirm the reliability of experimental observations during the cooling process. The computationally derived magnitude, spatial pattern, and temporal evolution of velocity (Fig. 2g), as well as flow directions and toroidal structure (Supplementary Fig. 7), closely match the experimental measurements. In this study, Buoyancy-driven convection dominates over interface Marangoni effects in the coupled convection. The ratio $Ra/Ma_{oa} = \rho_o g \beta_o L^2 / \gamma_{oa}$ reveals that their relative strengths depend on the characteristic length L , gravitational acceleration g , and fluid properties. Here, Ra/Ma_{oa} ranges from 30.92 to 31.59. Theoretical analysis suggests that the Marangoni effect could dominate in such coupled Marangoni natural convection with smaller characteristic lengths, microgravity environments, or fluids exhibiting stronger surface tension temperature sensitivity. Conversely, intentional suppression of Marangoni effects could be achieved by reversing these parametric modifications.

R–B–M convection is characterized by the formation of a hexagonal array of convection cells that develops above a critical temperature difference²¹. The bifurcation from conduction to convection is subcritical¹⁷. As the controlling dimensionless number increases further, this hexagonal pattern will lose stability^{25,26}. However, convection in this study sets in without an observable critical temperature difference—both Ra and Ma immediately drive flow upon increases. The evolution of correlation curves between dimensionless numbers and average velocity magnitudes under $T_0 = 75$ °C, obtained from time-dependent calculations, confirms this threshold-free behavior (Fig. 2e, f). Meanwhile, the convection cells remain stable throughout the cooling process. The symmetrical toroidal structures retain global continuity (one single dominant cell per phase) and exhibit no structural transitions. This stability arises because the maximum dimensionless number reached during cooling fails to exceed the critical threshold required for flow destabilization. Furthermore, a linear stability analysis was performed at the moment ($T_c = 71$ °C) of maximum temperature difference, when convective instability is most likely to occur, during the cooling process from $T_0 = 75$ °C (Supplementary Note 5). This analysis delineates the relationship between perturbation growth rate and mode number. The most unstable mode number of the flow field is identified as 2 (Supplementary Fig. 8a), and the corresponding critical dimensionless number and regime diagram are obtained (Supplementary Fig. 8b–d).

Migration of water molecules

Another intriguing phenomenon observed is the migration of water molecules into the oil phase, forming nanoscale water droplets,

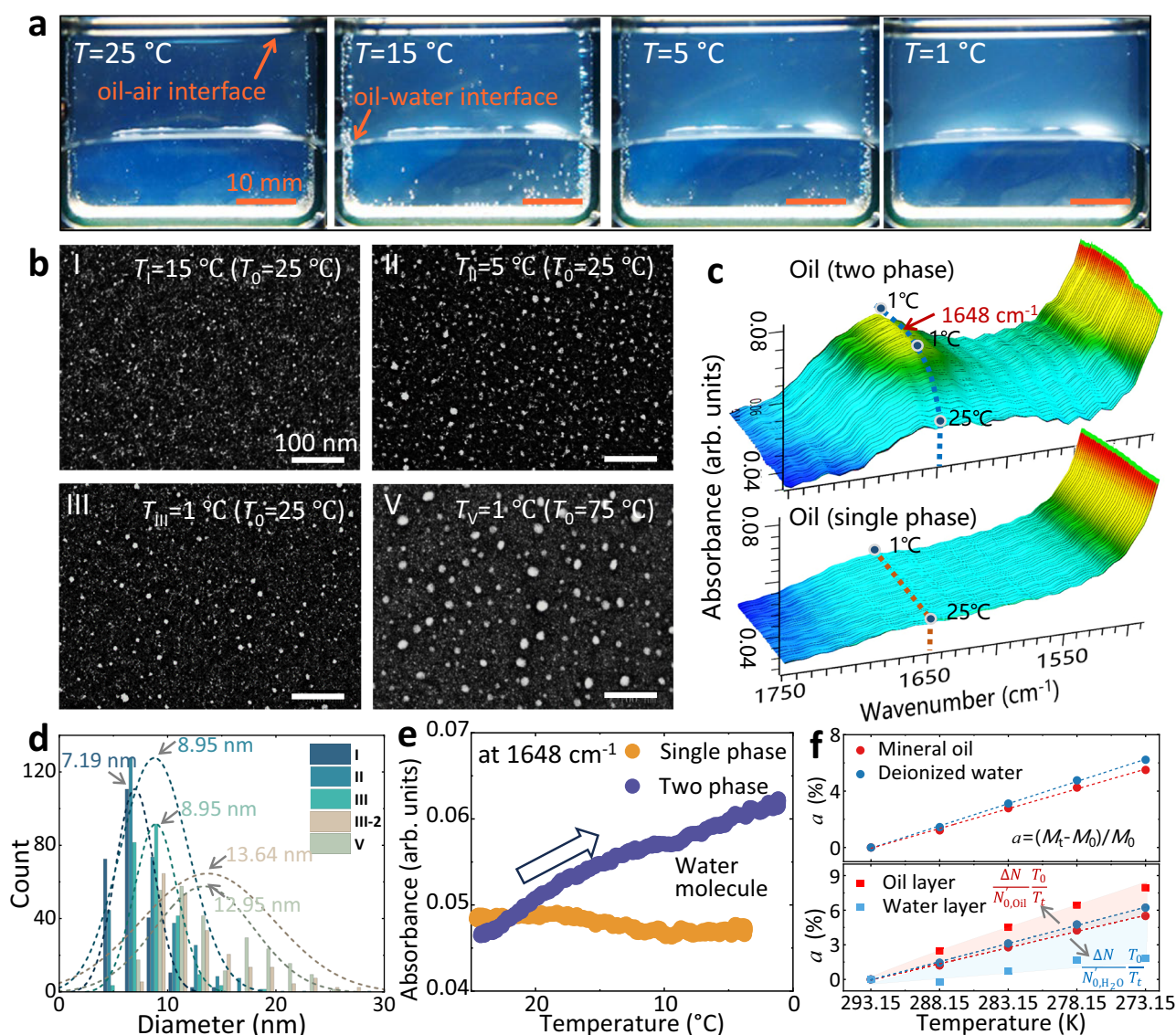


Fig. 3 | Demonstration of the presence of water nanodroplets. **a** Macroscopic view of oil and water layers during convection at various temperatures with $T_0 = 25^\circ\text{C}$. Upper layer: mineral oil. Lower layer: deionized water. Scale bar: 10 mm. **b** Images of water nanodroplets captured via transmission electron microscopy. The first three images and the fourth image were from two cooling tests: $25-1^\circ\text{C}$ and $75-1^\circ\text{C}$, respectively. Samples of images I–III were from 15, 5, 1°C , respectively. Samples of image V were from 1°C . Scale bar: 100 nm. **c** Three-dimensional infrared spectra of oil phase in two-phase (top) and single-phase (bottom) systems. Red and blue dashed lines indicate the infrared signals of 1648 cm^{-1} . Blue dots denote initial (25°C) and final (1°C) temperatures. **d** Particle size distribution of the droplets

from (b). The numbers indicate the average particle size of each sample. Dashed lines are the normal distribution of the particle size data. Sample III-2 was obtained from sample III after 36 h of standing. **e** Evolution of infrared absorption intensity at 1648 cm^{-1} of single phase and two phases during cooling from (c). The arrow denotes increasing water molecule concentration. **f** Evolution of the magnetization deviation ratio, α , with temperature. The top and bottom parts represent the single-phase and two-phase cooling tests, respectively. Red/blue areas indicate the increase and decrease of the magnetization deviation ratio of the oil/water phases, respectively.

during Marangoni natural convection. The existence of water nanodroplets in the oil phase is demonstrated via visualization, infrared spectroscopy, and hydrogen proton migration analysis. Figure 3a documents the opacity evolution of the biphasic system during cooling from $T_0 = 25^\circ\text{C}$. Progressive opacity development is observed in the oil phase (upper layer), with higher initial temperatures correlating to enhanced terminal opacity. Continuous infrared spectral measurements of mineral oil during cooling were performed using an in situ system (Supplementary Fig. 1d). For deionized water, the OH bending vibration of water molecules yields an absorption peak at 1640 cm^{-1} . By contrast, the mineral-oil spectrum exhibits no peak near 1640 cm^{-1} (Supplementary Fig. 5a, Supplementary Note 6). Therefore, the absorption peak at 1640 cm^{-1} of water is used as an

indicator of the presence of water molecules in the oil phase. A comparison of mineral-oil infrared spectra in single- and two-phase (mineral oil (50 ml), mineral oil and deionized water (25 ml each)) cooling tests ($25-1^\circ\text{C}$) reveals that the infrared signal at 1648 cm^{-1} is independent of temperature in the absence of water (Fig. 3c,e). In the two-phase system, mineral oil infrared spectra show a strengthening absorption peak with decreasing temperature at 1648 cm^{-1} , indicating a gradual increase in the number of water molecules (Fig. 3e). The existence of nanodroplets in the oil phase was identified via transmission electron microscope (TEM) (Fig. 3b). The average particle size of the nanodroplets increases with decreasing temperature (Fig. 3d). Because the lower temperature means a longer convection period, more water molecules enter the oil phase, yielding larger

droplets. The final average droplet size with $T_0 = 75^\circ\text{C}$ is 12.95 nm (Fig. 3bV), exceeding the 8.95 nm, which means the droplet size could be influenced by adjusting the duration of convection. Furthermore, nanodroplets persist after the sample is left for 36 h without surfactant, although their average size increases slightly (III-2 in Fig. 3d).

The migration of hydrogen protons in oil and water was analyzed using a ^1H low-field nuclear magnetic resonance (NMR) system (Supplementary Fig. 1c). The same heat-transfer environment with low- and high-thermal-conductivity bottom and sides, respectively, was obtained using a jacketed NMR chamber. The T_2 relaxation time evolution of deionized water, mineral oil, and oil + water during cooling is shown in Supplementary Fig. 5b–d (Supplementary Note 6). Temperature has a considerable effect on the shape and magnitude of the T_2 distributions. In transverse magnetization measurements, the spin echo train recorded using a Carr-Purcell-Meiboom-Gill sequence (Supplementary Note 1) did not decay with a single T_2 value but instead with a distribution of T_2 values. Through echo fitting, the echo train was mapped to a T_2 distribution, wherein the function of the echo amplitude with respect to time ($M = f(t)$) was transformed into a function of the volume over T_2 ($V = f(T_2)$). The area under the T_2 distribution curve equals the initial amplitude of the spin echo train, which is determined using Curie's law²⁷ as in Eq. (20).

$$M = \frac{N\gamma^2\hbar^2 I(I+1)\mathbf{B}_0}{3kT} \quad (20)$$

Curie's law prescribes the net magnetization M of a system of N spins with spin I and magnetogyric ratio γ observed in a static magnetic field \mathbf{B}_0 at temperature T . Further, k refers to the Boltzmann constant, and \hbar is the Planck constant. For single-phase (oil or water) cooling processes, the above parameters are constant except temperature T . Magnetization M (area under T_2 curves) is a single-valued function of $1/T$. To investigate the relationship between temperature and magnetization in various cooling tests, a dimensionless parameter a (magnetization deviation ratio) is defined to eliminate the differences in N .

$$a = \frac{M_t - M_0}{M_0} \quad (21)$$

M_t is the magnetization at moment t , M_0 is the initial magnetization, and a is a single-valued linear function of $1/T$. In the single-phase cooling tests, the a curves of oil and water show the same linearity and approximate values (Fig. 3f, top), consistent with theoretical calculations.

In the two-phase cooling tests, the a curves for the oil and water peaks reveal deviations opposite to those in the single-phase tests (Fig. 3f bottom). Because the difference in N is eliminated in Eq. (21), such deviations should not theoretically exist. Therefore, mass transfer occurs between the oil and water layers during cooling. The number of spins N in Eq. (20) is no longer a constant. The migration of water molecules into the oil phase reduces the number of spins in the water phase and improves N in the oil phase, which finally yields a larger value of M_t and a in the oil phase. The changed areas are indicated in blue and red (Fig. 3f). Furthermore, for the water peak, the spin number is the largest at the initial moment, that is, $N_{0,\text{H}_2\text{O}} > N_{t,\text{H}_2\text{O}}$. Noting that $\Delta N = N_{0,\text{H}_2\text{O}} - N_{t,\text{H}_2\text{O}}$, the a at time t is obtained as

$$a = \frac{M_{t,\text{H}_2\text{O}}}{M_{0,\text{H}_2\text{O}}} - 1 = \frac{T_0}{T_t} \cdot \frac{N_{0,\text{H}_2\text{O}} - \Delta N}{N_{0,\text{H}_2\text{O}}} - 1 = \frac{T_0}{T_t} - 1 - \frac{\Delta N}{N_{0,\text{H}_2\text{O}}} \cdot \frac{T_0}{T_t}, \quad (22)$$

where $\frac{\Delta N}{N_{0,\text{H}_2\text{O}}} \cdot \frac{T_0}{T_t}$ is the reduced portion of the water phase curve in Fig. 3f, which is zero for single-phase cooling tests. For the oil peak at the same moment t , its a is calculated as

$$a = \frac{M_{t,\text{Oil}}}{M_{0,\text{Oil}}} - 1 = \frac{T_0}{T_t} \cdot \frac{N_{0,\text{Oil}} + \Delta N}{N_{0,\text{Oil}}} - 1 = \frac{T_0}{T_t} - 1 + \frac{\Delta N}{N_{0,\text{Oil}}} \cdot \frac{T_0}{T_t}, \quad (23)$$

where $\frac{\Delta N}{N_{0,\text{Oil}}} \cdot \frac{T_0}{T_t}$ is the increased portion of the oil-phase curve. As the number of spins in deionized water is less than that in mineral oil at the initial moment ($N_{0,\text{H}_2\text{O}} < N_{0,\text{Oil}}$), the deviation of the water phase exceeded that of the oil phase at the same moment.

Mechanisms of directional water molecule transport

Nanoscale water droplets are generated during convection cell rotation owing to the combination of toroidal structure and interactions between oil and water molecules. At the oil-water interface, hydrogen bonding between adjacent water molecules is weak^{28,29}. Meanwhile, weak interactions exist between water and oil molecules, leading to a substantial orientation of the weakly hydrogen-bonded water molecules in the interfacial region. According to the findings of Richmond's team^{28,30}, in a free OH model, one OH bond and its companion orient toward the oil and water phases, respectively (Fig. 4aI). In a water monomer model, water molecules have negligible interactions among themselves, with their OH bonds pointing to the organic phase or entering the oil phase directly (Fig. 4aII). These OH models yield a sharp interfacial region within the dimensions of 5–10 Å. The molecular structure at the mineral oil-water and air-water interfaces was detected using a sum frequency generation (SFG, "Methods") spectrometer (Fig. 4b). Peaks appear at $\sim 3710\text{ cm}^{-1}$, corresponding to the free OH bonds of interfacial water molecules that straddle the interface and protrude to the organic or air phase. The sharpening of the SFG spectrum at the oil-water interface compared with the air-water interface is attributed to the strengthening of the OH oscillator due to decreased hydrogen bonding interactions among water molecules. Meanwhile, mineral oil is a mixture wherein different hydrocarbon molecules exhibit varied interactions with the OH groups of water molecules. The high-entropy environment induces a lower orientational order of OH than at the air-water interface. Simultaneous red and blue shifts lead to broadening of the band at $\sim 3710\text{ cm}^{-1}$. Furthermore, opposite flow directions between the bottom and top of the oil and water layers, respectively, generate friction at the oil-water interface (Fig. 4c). When interfacial water molecules spontaneously enter the oil phase, they are further entrained inside the bulk oil by convection. As the concentration increases, water molecules aggregate into droplets via hydrogen bonding, forming nanodroplets (Fig. 4c). Notably, the formation of analogous nanodroplets in the oil phase was not detected in the classical two-layer R-B convection system (refer to Supplementary Note 7 for detailed experimental validation).

Furthermore, the effects of initial temperature on water molecule transport are explored using an in situ infrared system (Supplementary Fig. 1d). The intensity of the infrared absorption peak at 1648 cm^{-1} is linearly correlated with the number of water molecules in oil phase (Figs. 3c and 4g). The three-dimensional infrared spectra (Fig. 4g) show that the signal intensity of water molecules progressively increases during cooling, reaches a maximum, and then stabilizes until cooling cessation. Comparative analysis reveals a significantly enhanced infrared absorption peak at higher initial temperatures (Fig. 4g) than at 25°C (Fig. 3c). Cross-temperature comparisons (Fig. 4d, e) confirm that elevated initial temperatures result in higher maximum intensities, indicating enhanced water transport into the oil phase. This phenomenon arises from the enhanced flow intensity (Fig. 4h, i) and prolonged duration of Marangoni natural convection at higher initial

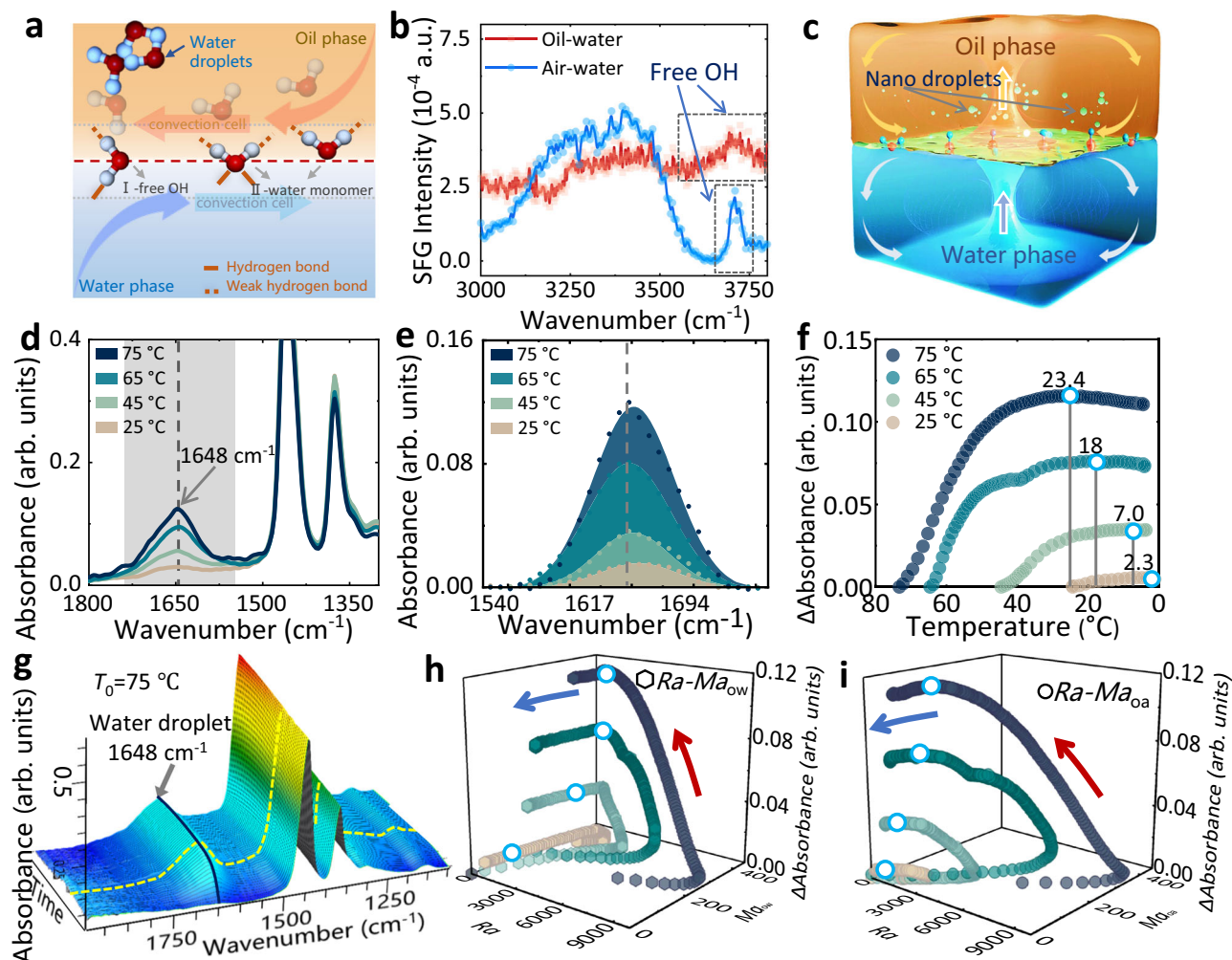


Fig. 4 | Mechanisms and influencing factors of water molecule transport driven by Marangoni natural convection. **a** Sketch of two OH-group models of water molecules at the oil-water interface. Upper layer: oil phase. Lower layer: water phase. The red dashed line represents the oil-water interface. Orange and blue arrows indicate the opposite flow direction of oil and water near the interface. Gray dashed lines represent the sharp interfacial region. **b** Sum frequency generation spectra of the oil-water and air-water interface in the range of 3000–3800 cm^{-1} under 20 °C. Gray dashed boxes: free OH peaks. **c** Schematic of convection cells in oil/water phases. Arrows: flow direction. The balls in the oil phase indicate nano droplets. Interfacial water molecules are identical to (a). **d** Comparison of infrared spectra (1300–1800 cm^{-1}) of oil phase at various T_0 . Gray band represents peak

width. **e** Local magnification (1530–1760 cm^{-1}) of peaks from (d) after spectra fitting. **f** Evolution of relative absorbance at 1648 cm^{-1} of the oil phase during cooling. $\Delta\text{Absorbance}$ is the absorption intensity after correction for the initial value. Temperatures corresponding to the maximum absorbance are labeled via white points and brown lines. **g** Three-dimensional infrared spectra of oil phase (two-phase cooling). The yellow dashed line indicates maximum absorbance. The black curve shows the evolution of absorbance at 1648 cm^{-1} . Coupled evolution of $Ma_{ow}(h)/Ma_{oa}(i)$, Ra , and $\Delta\text{Absorbance}$ (at 1648 cm^{-1}). The color-temperature correspondence is identical to that of (e, f). The white points correspond to those in (f). The red and blue arrows refer to stage I of rapid and stage II of slow water molecule transport, respectively.

temperatures under a fixed cooling rate, which synergistically accelerate water molecule transport and increase cumulative mass transfer. The temperature-dependent evolution of relative infrared signal intensity ($\Delta A.U.$) in Fig. 4f further corroborates this. The slopes of the curves quantify water transport rates: for a given T_0 , slope decay during cooling correlates with reduced convection intensity (Fig. 4h, i); across various T_0 conditions, steeper slopes at higher T_0 correspond to stronger convection. The relative signal values represent cumulative water transport, and prolonged convection durations at elevated T_0 result in significantly amplified infrared intensities.

Notably, the infrared signal reaches its maximum intensity before cooling termination (white dots in Fig. 4f, h, i) and subsequently stabilizes, indicating that water molecule transport ceases once the oil phase attains a saturation threshold, similar to fluid saturation in rock pores, despite ongoing convection. This saturation limit, which increases with initial temperature, is likely caused by thermal expansion of the oil phase at elevated temperatures. The water molecule

transport process comprises two distinct stages: I. Marangoni natural convection drives a rapid water influx into the oil phase, marked by a sharp increase in infrared absorption intensity. II. Under near-saturation conditions, only gradual molecular transport persists until the saturation threshold is reached.

Potential applications: emulsification

Building on these findings, the size distribution and temporal stability of nanodroplets in the oil phase were further characterized using dynamic light scattering (DLS, “Methods”) to assess the reliability of this Marangoni natural convection-based emulsification. It can be inferred that nanodroplets, formed by molecular agglomeration under a surfactant-free environment, inevitably coalesce under the combined effects of macroscopic convection and persistent Brownian motion. Once convection subsides, droplets exceeding the critical size for Brownian motion gradually sediment back into the aqueous phase through gravitational sedimentation.

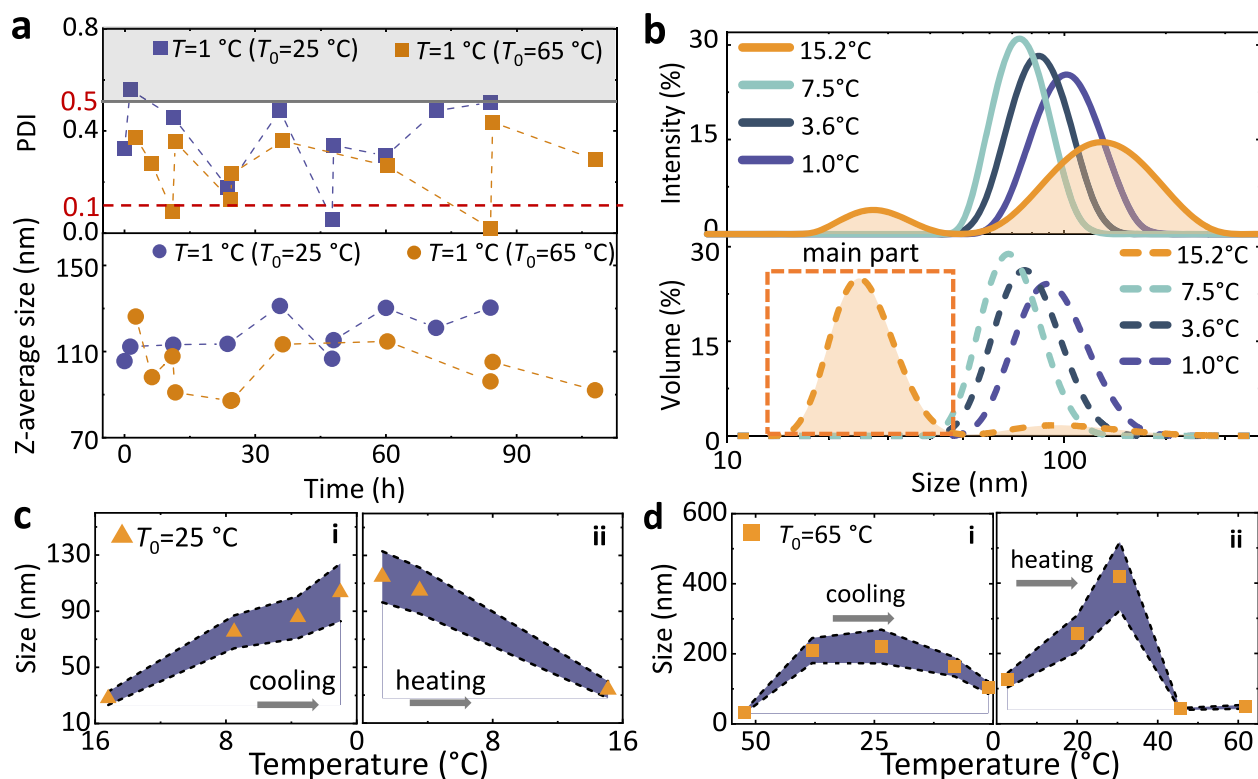


Fig. 5 | Dynamic light scattering analyses of water-in-oil nanoemulsions.

a Temporal evolution of the polydispersity index (PDI) and z-average size of water nanodroplets. Samples were measured at 1°C. Blue/orange symbols represent initial temperatures of 25°C and 65°C, respectively. The gray area indicates the comparability failure of PDI. A PDI below 0.1 (red dashed line) indicates that monodisperse distribution. **b** Droplet size distributions at selected temperatures during cooling. Solid lines: intensity-weighted size distributions; dashed lines:

volume-weighted size distributions. The orange dashed box indicates the dominant size range in samples. Orange shading emphasizes the bimodal distribution at 15.2°C. Evolution of mean droplet size versus temperature during heating and cooling cycles for $T_0 = 25^\circ\text{C}$ (**c**) and $T_0 = 65^\circ\text{C}$ (**d**). Blue-shaded regions represent error bands derived from connecting individual error bars. The gray arrows indicate the cooling and heating process.

The moment of convection cessation (i.e., when the temperature reaches 1°C) was taken as the temporal starting point to evaluate the nanodroplet lifetime. Figure 5a illustrates the temporal evolution of the polydispersity index (PDI) and z-average size of nanodroplets at 1°C. The two samples are from different initial temperatures: 25°C (blue points) and 65°C (orange points). Both PDI (ranging from 0.019 to 0.561) and z-average size (ranging from 87.11 to 131.2 nm) exhibit oscillatory behavior within fixed ranges over time. PDI values between 0 and 0.5 indicate acceptable comparability. The oscillatory trends of PDI and z-average size support the hypothesis that droplet dynamics involve continuous coalescence and settling. Dominance of coalescence leads to an increase in PDI and z-average size, whereas dominance of settling results in a reduction in both metrics as larger droplets sediment out of the oil phase. Furthermore, the z-average size of nanodroplets stabilizes near 110 nm over 84 ($T_0 = 25^\circ\text{C}$) and 108 ($T_0 = 65^\circ\text{C}$) h, respectively. Notably, nanodroplets remain in the oil phase at the end of the tests. Although complete emulsion breakdown via coalescence and settling is theoretically inevitable, this duration is considerably longer than anticipated.

Comparative analyses reveal that the initial temperature has no significant effect on droplet size (Fig. 5a), whereas the final temperature (as detailed in the “Methods”) has a much greater influence. Figure 5b displays the size distributions of droplets sampled at varying temperatures during cooling ($T_0 = 25^\circ\text{C}$). Due to convection effects, the droplet size follows a multimodal distribution with a high PDI (>0.5), exceeding the valid range for cumulant fitting algorithms. Therefore, the distribution analysis was employed to evaluate droplet size. However, in DLS, Rayleigh scattering intensity correlates exponentially with droplet diameter. For the 15.2°C sample, intensity-

weighted distributions overemphasize larger droplets (135.2 nm peak) compared to volume-weighted distributions (representative diameter = 27.94 nm). In this case, the small droplets are considered to constitute the major fraction of the sample (Fig. 5b). The size evolution during the heating (1°C→25°C) and cooling (65°C→1°C) cycles was also characterized (Supplementary Fig. 9).

The average droplet size progressively increases with decreasing temperature (Fig. 5ci), attributed to the continuous accumulation of water molecules in the oil phase during convection. For the higher initial temperature (Fig. 5di), the prolonged convection durations result in a larger maximum droplet size (220.9 nm). The nonlinear droplet size-temperature relationship (Fig. 5di) stems from water molecule saturation in the oil phase, as confirmed by infrared spectra results previously. In addition, heating had a significant effect on droplet size. For $T_0 = 25^\circ\text{C}$ (Fig. 5cii), the droplet size decreases with rising temperature, whereas for $T_0 = 65^\circ\text{C}$, the size initially increases before decreasing (Fig. 5dii). Elevated temperatures reduce oil viscosity and enhance Brownian motion, accelerating droplet coalescence, growth, and gravitational settling. Heating-induced nanodroplet destabilization at higher temperatures produces a broader size distribution compared to low-temperature conditions (expanded blue band in Fig. 5dii). Once larger droplets have settled, smaller droplets dominate the oil phase, as reflected in bimodal distributions (~10 to ~1000 nm) during heating (Supplementary Fig. 9a, b, e, f). This heating-induced destabilization also accounts for the discrepancy between DLS-measured sizes (~100 nm) and TEM results (~10 nm). During TEM sample preparation, despite lowering the ambient temperature, the ambient temperature remained higher than that of the droplets. These results demonstrate that nanodroplet size can be controlled by

regulating the final temperature. Furthermore, coordinated adjustment of both initial and final temperatures can mitigate the adverse effects associated with high-temperature conditions. For instance, initializing the system at 65 °C and cooling to 25 °C could prevent thermal destabilization under ambient environments.

Discussion

Unsteady physical fields, common in fluid mechanics, inherently induce potential disequilibrium, leading to the directional transport of substances. These motions are often spontaneous, self-organized, small-scale, and multifield-coupled. Historically, limited research tools have resulted in the oversimplification or neglect of these critical motions¹. For example, in deep-water hydrocarbon transport pipelines, alternating temperatures and natural surfactants create unsteady physical fields where oil, gas, and water coexist. During gas hydrate blockage, hydrates are often assumed to form at the oil-water interface^{31,32}. However, the results reported here suggest the possibility of hydrate formation at the gas-oil interface owing to the directional transportation of water molecules. Accurate identification of hydrate formation sites is essential to prevent and control blockages.

Driven by surface tension, this phenomenon is equally valid in microgravity environments^{15,21}. This directional molecular transport offers a stable, scalable, and controllable method for applications such as semiconductor film fabrication, high-purity crystal growth, nanoparticle monolayer fabrication, and targeted drug delivery^{33–35}. Considering the significant role of emulsions, particularly nanoemulsions, in food processing, cosmetics, and pharmaceuticals^{36,37}, novel emulsification technologies are continuously evolving^{3,38,39}. The Marangoni natural convection-based emulsification method described here meets industrial requirements: it is highly stable (persisting for more than 108 h without surfactants), scalable (applicable beyond mineral oil systems), and manageable (with droplet diameters tunable by temperature).

In conclusion, this study demonstrates that in an oil-water stratified system, a horizontal temperature gradient induces toroidal convection cells in both phases, driven by interfacial tension and density gradients. Hydrogen bonding between interfacial and bulk water molecules is weak. In the interfacial region, hydroxyl groups spontaneously penetrate the oil phase, interacting with oil molecules. The toroidal convection creates continuous friction at the interface, facilitating the transfer of weakly hydrogen-bonded water molecules into the oil phase until saturation. The difference between initial and final temperatures during the cooling process controls the extent of this molecular transport, highlighting its tunability. These findings provide fundamental insights into the dynamic processes of complex fluids, particularly those driven by transverse temperature gradients. The surfactant-free nature and tunability of this method make it ideal for directional transport applications.

Methods

Materials

The primary fluids used in experiments were mineral oil (Macklin, CAS: 8020–83–5, anhydrous, $\rho = 0.84$ g/ml at 25 °C) and deionized water. Detailed thermophysical properties of the mineral oil at different temperatures are provided in Supplementary Fig. 6. Tracer particles used in the 2D PIV system were polystyrene particles with a diameter of 15 μm and a density of 1.05 g/cm³. Fluorescent particles used in fluorescence microscopy experiments had an average diameter of 1–2 μm , a density of 1.1 g/cm³, an excitation wavelength of 532 nm, and an emission wavelength of 618 nm.

Main experimental systems

Four primary experimental systems were employed in this study: 2D PIV, inverted fluorescence microscopy, ¹H low-field NMR, and in situ infrared spectroscopy. Detailed configurations and procedures of each system are presented in Supplementary Fig. 1 and Supplementary Note 1.

A sealed heat-exchange environment with an approximately adiabatic bottom and thermally conductive sidewalls is essential to initiate Marangoni natural convection. To achieve this, we employed a hexahedral sapphire reactor (for the 2D PIV and in-situ infrared systems, Supplementary Fig. 1a, d), a jacketed reactor (for the inverted fluorescence microscopy system, Supplementary Fig. 1b), and a jacketed NMR chamber (Supplementary Fig. 1c). In the hexahedral sapphire reactor, two opposing sidewalls were replaced with transparent sapphire plates (25 W/(m·K)) to permit camera imaging; a removable metal lid sealed the top, the bottom was quartz glass with low thermal conductivity (0.35 W/(m·K)) and high transparency (for laser entering the liquid phase). The remaining walls were constructed from steel. The jacketed reactor similarly combined a quartz base with steel walls. The NMR chamber comprised an annular interlayer for circulating fluorinated oil and an internal reaction zone sealed by pistons; heat exchange occurred predominantly through the sidewalls. For temperature control, the sapphire reactor was submerged in an acrylic tank connected to a water bath, whereas the jacketed reactor and NMR chamber were regulated using circulating water and fluorocarbon oil, respectively.

PIV data processing

The pathline and velocity fields (Fig. 1b, d, Supplementary Fig. 3) are instantaneous measurements calculated from two consecutive frames (1-s interval) using PIVlab software (version 2.63). The PIV system was calibrated to a pixel resolution of 40 $\mu\text{m}/\text{px}$. Displacements were calculated using the Gauss 2 × 3-point subpixel estimator in PIVlab, with a theoretical uncertainty of ± 0.05 px, corresponding to ± 2 μm or $\pm 2 \times 10^{-5}$ m/s velocity error. In Fig. 1d and Supplementary Fig. 3, the vector lengths represent relative length (cm/magnitude), specified as the number of centimeters per unit of vector magnitude. The scaling factor is set to 4000 in Fig. 1d and 14,000 in Supplementary Fig. 2.

Transmission electron microscopy test

A JEM-1200EX TEM microscope (Japan Electronics Corporation) was used to observe the water nanodroplets in the oil phase. The accelerating voltage was 100 kV, the magnification of the samples was one million times, and the point resolution was 0.14 nm. Samples were prepared using a negative staining method to enhance contrast as follows: (i) A sealing film was spread flat on a glass sheet, and a copper mesh was placed over the sealing film using forceps. Ten microliters of the sample were dropped onto the copper mesh via a pipette. After waiting for 10 min, the sample was stabilized. Excess liquid was removed using filter paper. (ii) Ten microliters of uranyl acetate (3 wt %) were dropped onto this copper mesh using a pipette. After waiting for 3 min, the excess liquid was removed using filter paper. (iii) Placed this copper mesh in the specimen holder for observation.

Sum frequency generation test

The SFG spectrometer was built by Ekspla based on Nd:YAG picosecond laser system. A co-propagating configuration was used. The visible light pulse was 532 nm, and the IR pulse was adjustable, ranging from 1000 to 4000 cm⁻¹. The incident angles were 60° and 55° for the visible and IR beams, respectively. The energy of visible and IR beams is generally less than 200 μJ . The ssp polarization combination (s-polarized sum frequency signal, s-polarized visible light pulse, and p-polarized IR pulse) was used in the oil-water interface measurements. For the SFG measurements, two lights, spatially and temporally overlapping, were directly shone on the interface of interest, and the generated sum-frequency light was directed to the detector through a series of filters and a polarization analyzer.

Dynamic light scattering measurements

All DLS measurements were performed using a Nano-ZS90 instrument (Malvern Instruments Ltd., UK) with a detectable size range of 2 nm to 3 μm . A square quartz cuvette (1.5 mL sample volume per test) was

used, with 20 runs per measurement. For temporal stability assessment, the onset of nanodroplet lifetime tracking commenced when the system temperature reached 1 °C. Samples were periodically collected from the sapphire reactor immersed in the water tank (Supplementary Fig. 1). During each sampling, the reactor was carefully extracted from the water tank, quickly sampled, and then rapidly resealed and returned to the water. Additionally, before each sampling, quartz cuvettes were pre-cooled to the target temperature (1 °C) to mitigate thermal degradation. For sampling during the heating/cooling cycles, system temperature was monitored in real time using a temperature probe. Once the system reached sampling temperature, the aforementioned procedure was repeated. These sampled temperatures were treated as the final temperatures of Marangoni natural convection for comparative analysis of droplet-size dependence.

Measurements of mineral oil properties

The thermophysical properties of mineral oil at various temperatures are required to calculate the dimensionless numbers, which include density, temperature coefficients of interfacial tension, kinetic viscosity, and thermal diffusivity. The density was measured over 0–80 °C using a densimeter D4 (Mettler Toledo, Switzerland), with a measurement resolution of 0.0001 g/cm³ and an accuracy of ± 0.0001 g/cm³. The oil-air interfacial tension was measured from 1 to 80 °C via a tensiometer K100 (KRÜSS, Germany) using the Wilhelmy hanging plate method, with a measurement resolution of 0.002 mN/m. The oil-water interfacial tension was measured via the pendant drop method across eight temperature points (5.7–73.9 °C). The rheometer (MCR 302), manufactured by Anton Paar in Austria, was employed to measure the dynamic viscosity over 0–80 °C. The light flash apparatus (LFA 467) manufactured by Netzsch in Germany was used to measure the thermal diffusivity over 0–80 °C. The measurement accuracy was $\pm 3\%$, repeatability was $\pm 2\%$, and the sample rate was 2 MHz. A sample container with a lid for low-conductivity liquids made of aluminum/stainless steel was used for the test.

Data availability

The authors declare that the data that support the findings of this study are available in the main article, the Supplementary Information, and the Source data file. Source data are provided with this paper.

References

- Lohse, D. & Zhang, X. Physicochemical hydrodynamics of droplets out of equilibrium. *Nat. Rev. Phys.* **2**, 426–443 (2020).
- Keiser, L., Bense, H., Colinet, P., Bico, J. & Reyssat, E. Marangoni bursting: evaporation-induced emulsification of binary mixtures on a liquid layer. *Phys. Rev. Lett.* **118**, 074504 (2017).
- Colón-Quintana, G. S., Clarke, T. B. & Dick, J. E. Interfacial solute flux promotes emulsification at the water/oil interface. *Nat. Commun.* **14**, 705 (2023).
- Wodlei, F., Sebilliau, J., Magnaudet, J. & Pimienta, V. Marangoni-driven flower-like patterning of an evaporating drop spreading on a liquid substrate. *Nat. Commun.* **9**, 820 (2018).
- Park, S. et al. Solutal Marangoni effect determines bubble dynamics during electrocatalytic hydrogen evolution. *Nat. Chem.* **15**, 1532–1540 (2023).
- Scriven, L. E. & Sternling, C. V. The Marangoni effects. *Nature* **187**, 186–188 (1960).
- Yunker, P. J., Still, T., Lohr, M. A. & Yodh, A. G. Suppression of the coffee-ring effect by shape-dependent capillary interactions. *Nature* **476**, 308–311 (2011).
- Larson, R. G. Twenty years of drying droplets. *Nature* **550**, 466–467 (2017).
- Rey, M. et al. Versatile strategy for homogeneous drying patterns of dispersed particles. *Nat. Commun.* **13**, 2840 (2022).
- Cira, N. J., Benusioglio, A. & Prakash, M. Vapour-mediated sensing and motility in two-component droplets. *Nature* **519**, 446–450 (2015).
- Frank, B. D. et al. Reversible morphology-resolved chemotactic actuation and motion of Janus emulsion droplets. *Nat. Commun.* **13**, 2562 (2022).
- Li, Y. et al. Oil-on-water droplets faceted and stabilized by vortex halos in the subphase. *Proc. Natl. Acad. Sci. USA* **120**, e2214657120 (2023).
- Kim, H., Muller, K., Shardt, O., Afkhami, S. & Stone, H. A. Solutal Marangoni flows of miscible liquids drive transport without surface contamination. *Nat. Phys.* **13**, 1105–1110 (2017).
- Xiao, Y. et al. Generation of Fermat's spiral patterns by solutal Marangoni-driven coiling in an aqueous two-phase system. *Nat. Commun.* **13**, 7206 (2022).
- Napolitano, L. G. Marangoni convection in space microgravity environments. *Science* **225**, 197–198 (1984).
- Nield, D. A. Surface tension and buoyancy effects in cellular convection. *J. Fluid Mech.* **19**, 341–352 (1964).
- Juel, A., M. Burgess, J., McCormick, W. D., Swift, J. B. & Swinney, H. L. Surface tension-driven convection patterns in two liquid layers. *Phys. D Nonlinear Phenom.* **143**, 169–186 (2000).
- Simanovskii, I. & Nepomnyashchy, A. *Convective Instabilities in Systems with Interface* (Gordon and Breach, 1993).
- Pandey, A., Scheel, J. D. & Schumacher, J. Turbulent superstructures in Rayleigh-Bénard convection. *Nat. Commun.* **9**, 2118 (2018).
- Trowbridge, A. J., Melosh, H. J., Steckloff, J. K. & Freed, A. M. Vigorous convection as the explanation for Pluto's polygonal terrain. *Nature* **534**, 79–81 (2016).
- Nepomnyashchy, A., Simanovskii, I. & Legros, J. *Interfacial Convection in Multilayer Systems* (Springer, 2012).
- Liu, H.-R., Chong, K. L., Yang, R., Verzicco, R. & Lohse, D. Heat transfer in turbulent Rayleigh-Bénard convection through two immiscible fluid layers. *J. Fluid Mech.* **938**, A31 (2022).
- Bodenschatz, E., Pesch, W. & Ahlers, G. Recent developments in Rayleigh-Bénard convection. *Annu. Rev. Fluid Mech.* **32**, 709–778 (2000).
- Nepomnyashchy, A. & Simanovskii, I. Marangoni waves in two-layer films under the action of spatial temperature modulation. *J. Fluid Mech.* **805**, 322–354 (2016).
- Nepomnyashchy, A. & Simanovskii, I. Generation of nonlinear Marangoni waves in a two-layer film by heating modulation. *J. Fluid Mech.* **771**, 159–192 (2015).
- Simanovskii, I. & Nepomnyashchy, A. Nonlinear development of oscillatory instability in a two-layer system under the combined action of buoyancy and thermocapillary effect. *J. Fluid Mech.* **555**, 177–202 (2006).
- Kinney, D. R., Chuang, I. S. & Maciel, G. E. Water and the silica surface as studied by variable-temperature high-resolution ¹H NMR. *J. Am. Chem. Soc.* **115**, 6786–6794 (1993).
- Scatena, L. F., Brown, M. G. & Richmond, G. L. Water at hydrophobic surfaces: weak hydrogen bonding and strong orientation effects. *Science* **292**, 908–912 (2001).
- Shi, L. et al. Water structure and electric fields at the interface of oil droplets. *Nature* **640**, 87–93 (2025).
- Moore, F. G. & Richmond, G. L. Integration or segregation: How do molecules behave at oil/water interfaces?. *Acc. Chem. Res.* **41**, 739–748 (2008).
- Bassani, C. L., Sum, A. K., Herri, J.-M., Morales, R. E. M. & Cameirao, A. A multiscale approach for gas hydrates considering structure, agglomeration, and transportability under multiphase flow conditions: II. Growth kinetic model. *Ind. Eng. Chem. Res.* **59**, 2123–2144 (2020).

32. Aman, Z. M. & Koh, C. A. Interfacial phenomena in gas hydrate systems. *Chem. Soc. Rev.* **45**, 1678–1690 (2016).
33. Piñan Basualdo, F. N., Bolopion, A., Gauthier, M. & Lambert, P. A microrobotic platform actuated by thermocapillary flows for manipulation at the air–water interface. *Sci. Robot.* **6**, eabd3557 (2021).
34. Zhang, T. et al. In situ design of advanced titanium alloy with concentration modulations by additive manufacturing. *Science* **374**, 478–482 (2021).
35. Lin, X. et al. Marangoni effect-driven transfer and compression at three-phase interfaces for highly reproducible nanoparticle monolayers. *J. Phys. Chem. Lett.* **11**, 3573–3581 (2020).
36. Fryd, M. M. & Mason, T. G. Advanced nanoemulsions. *Annu. Rev. Phys. Chem.* **63**, 493–518 (2012).
37. Yin, N. et al. Polydopamine-based nanomedicines for efficient antiviral and secondary injury protection therapy. *Sci. Adv.* **9**, eadf4098 (2023).
38. Feng, J. et al. Nanoemulsions obtained via bubble-bursting at a compound interface. *Nat. Phys.* **10**, 606–612 (2014).
39. Guha, I. F., Anand, S. & Varanasi, K. K. Creating nanoscale emulsions using condensation. *Nat. Commun.* **8**, 1371 (2017).

Acknowledgements

This work is supported by the National Natural Science Foundation of China (Grant Nos. 52476058, L.X.Z.). A.H. acknowledges funding from KCCS through the AssureFlow-CCS and CRYSTAL-CCS projects.

Author contributions

Conceptualization: J.G.W., L.X.Z., J.F.Z., Y.C.S., methodology: J.G.W., L.X.Z., Y.C.S., X.S., investigation: J.G.W., L.X.Z., X.S., visualization: J.G.W., L.X.Z., A.H., supervision: L.X.Z., Y.L., Y.C.S., writing—original draft: J.G.W., writing—review and editing: J.G.W., L.X.Z., X.S., A.H.

Competing interests

The authors declare no competing interests.

Additional information

Supplementary information The online version contains supplementary material available at <https://doi.org/10.1038/s41467-025-60930-y>.

Correspondence and requests for materials should be addressed to Lunxiang Zhang or Yongchen Song.

Peer review information *Nature Communications* thanks Ilya B. Simanovskii and the other, anonymous, reviewers for their contribution to the peer review of this work. A peer review file is available.

Reprints and permissions information is available at <http://www.nature.com/reprints>

Publisher's note Springer Nature remains neutral with regard to jurisdictional claims in published maps and institutional affiliations.

Open Access This article is licensed under a Creative Commons Attribution-NonCommercial-NoDerivatives 4.0 International License, which permits any non-commercial use, sharing, distribution and reproduction in any medium or format, as long as you give appropriate credit to the original author(s) and the source, provide a link to the Creative Commons licence, and indicate if you modified the licensed material. You do not have permission under this licence to share adapted material derived from this article or parts of it. The images or other third party material in this article are included in the article's Creative Commons licence, unless indicated otherwise in a credit line to the material. If material is not included in the article's Creative Commons licence and your intended use is not permitted by statutory regulation or exceeds the permitted use, you will need to obtain permission directly from the copyright holder. To view a copy of this licence, visit <http://creativecommons.org/licenses/by-nc-nd/4.0/>.

© The Author(s) 2025